Monthly Notices of the ROYAL ASTRONOMICAL SOCIETY

MNRAS **515,** 2088–2098 (2022) https://doi.org/10.1093/mnras/stac1921
Advance Access publication 2022 July 11

Sporadic micro-meteoroid source radiant distribution inferred from the Arecibo 430 MHz radar observations

Yanlin Li,[1]★ Qihou Zhou,[2]★ Julio Urbina[1] and Tai-Yin Huang[3]

[1]*Department of Electrical and Computer Engineering, The Pennsylvania State University , University Park, PA 16802, USA*
[2]*Department of Electrical and Computer Engineering, Miami University, Oxford OH 45056, UK*
[3]*Department of Physics, the Pennsylvania State University, Lehigh Valley, PA 18034, USA*

Accepted 2022 July 4. Received 2022 May 24; in original form 2022 March 28

ABSTRACT

This work presents the result of sporadic meteor radiant density distribution using the Arecibo 430 MHz incoherent scatter radar (ISR) located in Puerto Rico for the first time. Although numerous meteor studies have been carried out using the Arecibo ISR, meteoroid radiant density distribution has remained a mystery as the Arecibo radar cannot measure vector velocity. A numerical orbital simulation algorithm using dynamic programming and stochastic gradient descent is designed to solve the sporadic meteoroid radiant density and the corresponding speed distributions of the meteors observed at Arecibo. The data set for the algorithm comprises over 250 000 meteors from Arecibo observations between 2009 and 2017. Five of the six recognized sporadic meteor sources can be identified from our result. There is no clearly identifiable South Apex source. Instead, there is a broad distribution between $+/-30^\circ$ ecliptic latitude, with the peak density located in the North Apex direction. Our results also indicate that the Arecibo radar is not sensitive to meteors travelling straight into or perpendicular to the antenna beam but is most sensitive to meteors with an arrival angle between 30° and 60°. Our analysis indicates that about 75 per cent of meteoroids observed by the Arecibo radar travel in prograde orbits when the impact probability is considered. Most of the retrograde meteoroids travel in inclined low-eccentricity orbits.

Key words: interplanetary medium – meteorites, meteors, meteoroids – zodiacal dust.

1 INTRODUCTION

As a meteoroid travels through the Earth's atmosphere, the intensive heat generated by the friction between the meteoroid and atmosphere can reach several thousands of degrees. The plasma surrounding the meteoroid created by the high temperature can be detected by ground-based radar systems typically between 80 and 130 km as meteors. The Doppler velocity of the meteor echoes is essentially the same as its parent body, i.e. the meteoroid allowing us to study meteoroid orbital characteristics using meteor echoes. The meteoroid population is broadly classified as shower or sporadic meteoroids. The former generally originates from comets or asteroids and behaves as a stream of particles with similar radiant direction and velocity (Halliday, Blackwell & Griffin 1990; Babadzhanov & Obrubov 1992; Wheeler et al. 2018). Sporadic meteoroids are not directly associated with a parent source, and they can be detected at any time of the year. Sporadic meteors by far dominate the meteoroid flux on to the Earth. Plane (2004) estimated the daily cosmic dust input to be nearly 300 tones d^{-1}. In the last two decades, all major high-power large aperture radars and many smaller radars have been used for meteor observations (e.g. Pellinen-Wannberg et al. 1998; Zhou, Mathews & Nakamura 2001; Close et al. 2002; Janches et al. 2003; Campbell-Brown & Jones 2006; Seal & Urbina 2020; Yue et al. 2020; Schult et al. 2021). The combined results of decades of observations suggest that sporadic meteors mainly originate from the following six sources: North and South Apex, North and South Toroidal, Helion, and Anti-Helion (Campbell-Brown & Jones 2006; Chau, Woodman & Galindo 2007; Szasz et al. 2008; Kero et al. 2012). Nesvorný et al. (2011) suggested that the meteors of the Apex sources originated from Oort Cloud comets. The orbital model of Pokorný et al. (2014) indicates the evolved Halley-type comets can be the source of the toroidal sources.

The Arecibo 430 MHz radar system is commonly referred to as the Arecibo incoherent scatter radar (ISR), which unfortunately collapsed in 2020 December (Witze 2020). The high sensitivity of the Arecibo ISR allowed the detection of the faintest meteor among any ground-based observations (Zhou, Tepley & Sulzer 1995). Mathews et al. (2001) used deceleration to arrive a limiting meteor mass of 10^{-14} kg, while Li & Zhou (2019) estimate the typical mass to be around 10^{-13} kg based on flux rate. Those estimates are based on various simplified assumptions and are subject to errors due to complexity in beam pattern, aspect sensitivity, radiant direction, and other factors. The monostatic Arecibo radar is not equipped with multiple baselines for interferometry, hence lacking the ability to retrieve 3D vector speed information from the target to measure radiant distribution directly. Several previous studies have modelled meteor input based on speed and flux characteristics of the Arecibo meteors from the sporadic source regions (Janches et al. 2006; Fentzke & Janches 2008; Fentzke, Janches & Sparks 2009) and from zodiacal dust cloud (Janches et al. 2014). However, these studies were focusing on limited aspect of either speed or flux characteristics. This

★ E-mail: yxl875@psu.edu (YL); zhouq@miamiOH.edu (QZ)

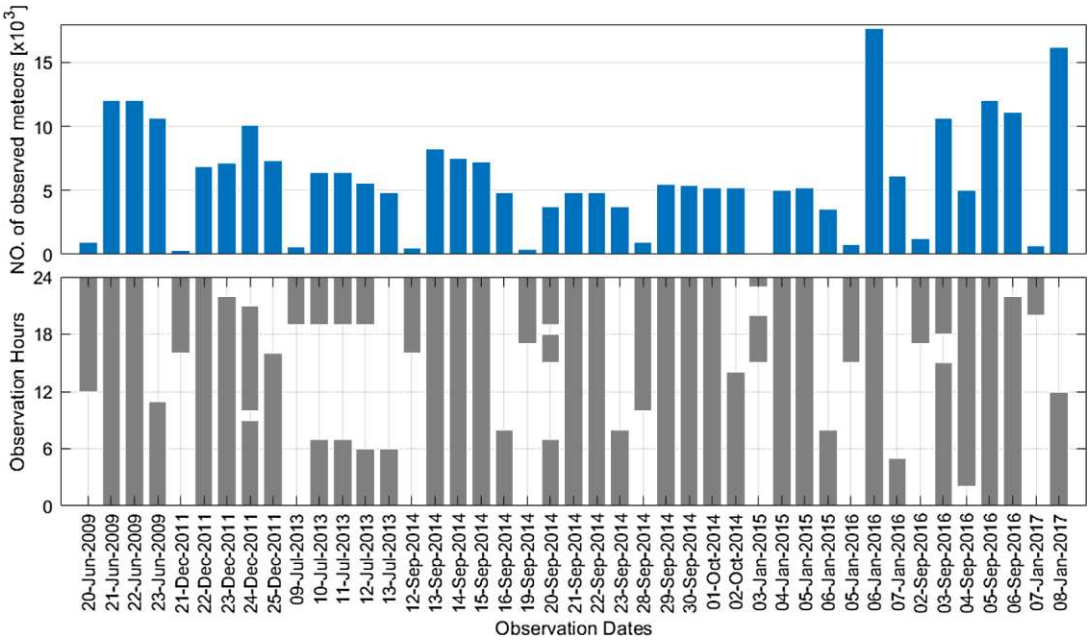

Figure 1. Daily number of meteors detected at each campaign (top) and local time of observation on each day (bottom) of each campaign. The hours covered by the grey bar indicate when the radar was in operation.

work reports the first sporadic meteor radiant density distribution that matches observations from July, September, and December simultaneously. An algorithm that comprises a meteoroid-Earth impact model and machine learning techniques is developed to inversely solve the 3D sporadic meteor radiant sources based on many meteor echoes observed by the Arecibo radar. The algorithm uses a stepwise stochastic gradient descent method to make the radiant densities most compatible with the observations.

This paper is organized as follows. First, we describe the data set used in our work and discuss the techniques involved in modelling the radiant source distribution. Following that, we report the results of Arecibo's meteoroid radiant density and speed distributions. Last but not least, we discuss the impact probability and its role in solving the radiant density distribution. This paper presents the first meteoroid radiant density distribution for the Arecibo ISR. With impact probability correction, our results could picture the actual orbital distributions of interplanetary particles near Earth.

2 METEOR HEAD ECHO DATA SET

The meteor data used in this report are obtained from 685 h of observations in 43 d. Those meteor campaigns were carried out in December, July, and September between 2009 and 2017. In total, the data sets contain 255 214 meteor head echoes. Fig. 1 shows the number of meteors detected in each experiment as well as the radar observation hours in each day. Some campaigns observed significantly less meteor head echoes, e.g. 2009 January 20, 2013 July 10, because the radar was not in operation near 6 AM when the meteor flux is at its maximum.

The Arecibo ISR usually interlaced multiple pulse schemes. This paper uses only data from the code-long-pulse (CLP) as described in Sulzer (2004) with a 10-ms inter-pulse-period (IPP) to ensure consistent sensitivity in all data sets (Zhou 2000). Although the 10 ms IPP CLP observation misses about 50 per cent of the meteors that last less than 5 ms, CLP is still by far the most sensitive pulse scheme for the Arecibo ISR due to its high compression ratio. On average, Arecibo observes about 50 meteors per minute near dawn and less than five meteors per minute at dusk. Meteor detections using the CLP scheme have been discussed in other works such as Li & Zhou (2019) and Li et al. (2020). The diurnal meteor flux rate in a typical day is similar to those found in Li & Zhou (2019). For this work, we create three groups with centre dates on July 1, September 15, and January 1. The meteors in our data set are allocated into the group with the closest centre date to their observation date. None of the observation dates deviates from its nearest centre date by more than 10 d. The rate of meteors observed as a function of local time and velocity is normalized to the radar operation time and calibrated to the noise background at each time slot.

Fig. 2 shows an example time-velocity-density plot before and after calibration with the September data. The left figure shows the original September group's time-velocity-density plot with the normalized time and superimposed noise calibration. The time calibration is proportional to the radar operation time within its time slot. We also perform a noise calibration to make the flux rate free from the effect of the time variation of the overall noise level. Each time slot's 'local' noise baseline is acquired by 10 min' moving average of the background power between 90 and 120 km. The ratio of the 'local' noise to the average noise between 12 AM and 4 AM, when the overall noise level is low, of the current data set is the noise calibration factor shown in the left-hand panel of Fig. 2. By dividing the time and noise calibration factors from the original result, we obtain the calibrated result shown on the right-hand side of Fig. 2.

3 ALGORITHM

In this work, we have developed an algorithm based on data obtained from Arecibo. The model is built upon the stochastic gradient descent method (LeCun et al. 2012) with both forward selection and backward elimination to solve the Arecibo meteor radiant distribution. In essence, solving Arecibo's radiant densities from the radar time sequence is an optimization problem. The goal is to find the optimal solution that is most compatible with all the

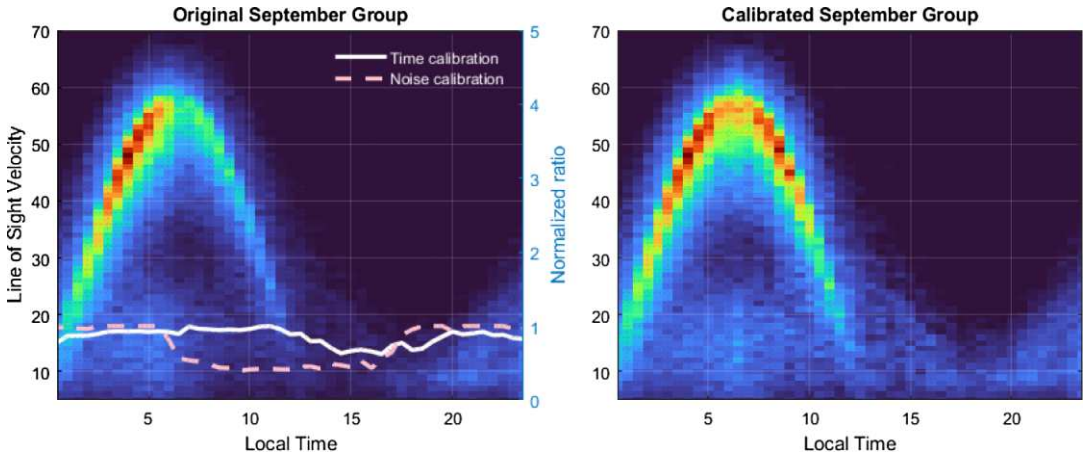

Figure 2. Time-velocity-density plot from the September group before (left) and after (right) calibration. Calibrations are made based on the effective radar time transmitting the coded-long pulse (solid line in the left figure) and the daily noise power variations (dashed line in the left figure).

observations. The algorithm developed is relatively demanding in processing power. We use a computer cluster of about 100 cores with Intel i5, i7, i9, and AMD Ryzen 9 processors. The whole project uses between 200 and 300 thousand core hours to complete the analysis.

Despite using a cluster, the algorithm still needs to be carefully optimized. Given the complexity of the objective, processing speed and efficiency are the keys. In this work, the Arecibo meteor radiant densities are solved using many small steps. Doing so reduces memory requirements by a wide margin and increases processing speed exponentially. Otherwise, the data involved require more than 100 GB of memory space on each computational node.

The algorithm consists of three major parts: seeding, dictionary, and the solver. While solving for radiant distribution, it also solves the Arecibo aspect sensitivity for the meteor head echoes.

3.1 Seeding

In our model, all meteoroids originate from a 'spawning sphere', placed at 10 times the Earth's radius away from the centre of the Earth. The spawning sphere has an escape velocity of 0.317 of that at Earth's surface. Placing the spawning sphere further away from the Earth returns more accurate results as doing so simulates the Earth's gravitational acceleration more accurately. However, the simulation complexity of $O(n^3)$ (Chivers & Sleightholme 2015) in 3D space prevents us from expanding the spawning sphere's radius indefinitely. There will be a rapidly diminishing return in using a larger spawning sphere.

At the start of the seeding process, meteoroids are placed on the spawning sphere in uniform distribution. An impact is recorded when a meteoroid reaches a ring area that is 100 km in height and 1° wide in latitude above the Arecibo Observatory (AO). In other words, meteoroids ending up between 17.5° N and 18.5° N, 100 km above sea level, are recorded as an impact in the seeding simulation. When a meteoroid reaches the detection ring, the longitude of the impact location is equivalent to Puerto Rico's local time. For example, the meteoroid impact at the apex direction, towards which the Earth is moving, is equal to the meteor head echoes detected at 6 AM in the seeding simulation.

The trajectories of the meteoroids between the spawning sphere and the impact are calculated with the adaptive semi-implicit Euler method (Hairer, Lubich & Wanner 2003). There are always $2^{15} = 32\,768$ meteoroids in the simulation, maintaining a fixed memory allocation. The number of meteoroids is chosen in consideration of the memory constraints of each processing node and the overall processing speed. Generally, a computer handles a matrix size that is the power of 2 the fastest, succeeded by even numbers, then by odd numbers. Meteoroids are removed once they reach the detection ring or move away from Earth. In the next iteration, meteoroids are immediately respawned on the spawning sphere to maintain the memory allocation for better computational efficiency. More than 99 per cent of the meteoroids in the simulation will not reach Earth.

The seeding process is divided into many batches. Each batch contains only a single speed from a single radiant direction. The seeding process for each season group includes $181 \times 91 \times 16 = 263\,536$ batches that cover all possible directions around Earth with a 2-deg step size on longitude (−180°–180°) and latitude (−90°–90°), and a 2 km s^{-1} step size on velocity from 10 to 40 km s^{-1}. Each batch ran for 20 000 steps to simulate the number of impacts within a fixed time interval. Each season group contains between 100 and 500 million meteoroids. It is essential to point out, instead of the number of meteoroids, the terminating criteria of each batch is defined by the number of time-steps because the probability of impact varies among different directions and speeds (Mathias, Wheeler & Dotson 2017).

Fig. 3 shows the impact probability of a meteoroid ending up on Earth in all directions and speeds for July, September, and December. Naturally, the collisional probability depends on the meteoroid's orbital parameters. For illustrative purposes, in Fig. 3, we show the radiant impact probabilities in low-, mid-, and high-speed groups. The impact probabilities of Apex sources (∼0° ecliptic longitude) are up to four times higher than anti-apex sources (∼180° or ∼−180° ecliptic longitude) for all speeds. The concentration leans to the north as AO is at 18° N latitude. During all the observations, the Arecibo radar pointed in the zenith direction (note also that the Arecibo radar had a full beam width of 1/6 deg). Since Earth's rotating axis is tilted 23° away from the normal of the ecliptic plane, the radar points at 41° above the ecliptic plane at mid-night and 5° at noon in July. The AO's pointing direction is 5° at mid-night and 41° at noon in December observations. The difference in pointing direction makes the shape of the concentrated area appear to be slanted in July and December results. In September, Arecibo's pointing is symmetric with respect to local mid-night and noon. Hence, the impact probability in September is symmetric with 0° and 180°

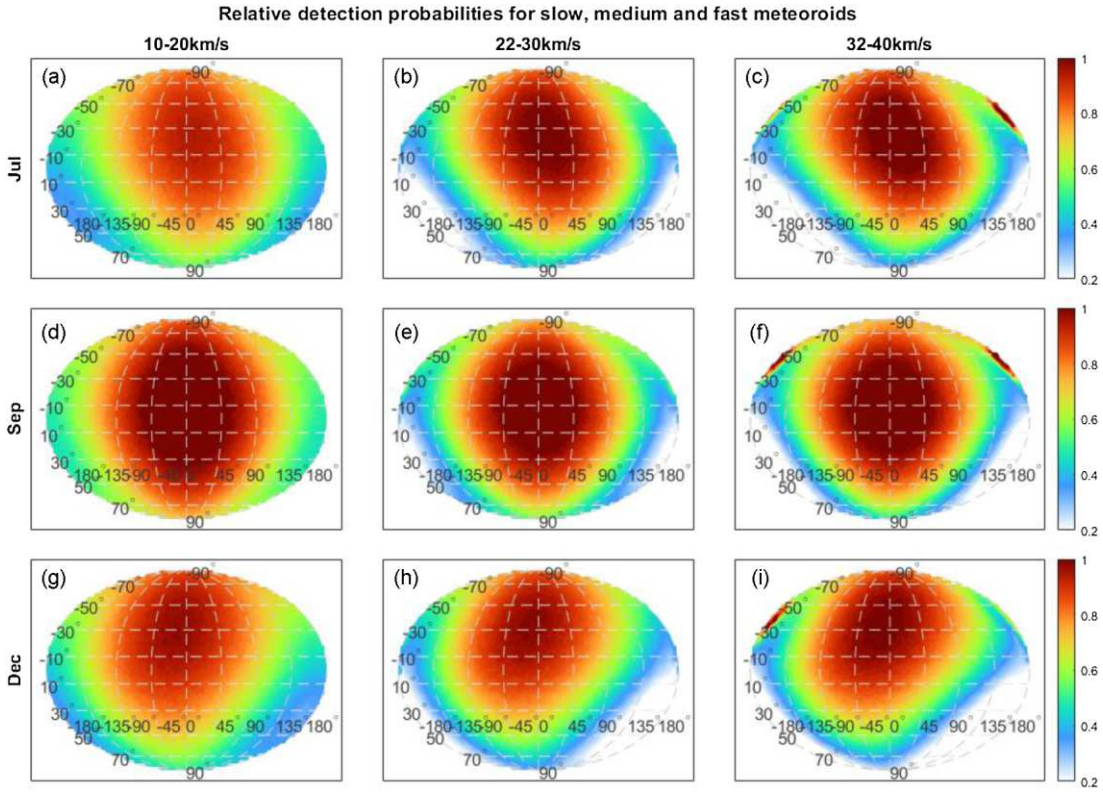

Figure 3. Relative impact probabilities under uniform radiant distribution in the solar reference frame (SRF) for July, September, and December in three velocity groups. The colour indicates the impact probability. The nine figures are combinations of July, September, December simulation and meteoroid speed of 10–20 km s^{-1} (low speed), 22–30 km s^{-1} (mid speed), and 32–40 km s^{-1} (high speed).

longitude. The meteoroids in identical or near-identical orbits to the Earth, i.e. relatively stationary to the Earth, will eventually end up on Earth due to gravitational acceleration. Very few orbits can satisfy such conditions; therefore, only an isolated bright spot can be found in the plots of the 22–30 km s^{-1} column at (180,0) or (−180,0). Two bright shoulder areas near (180°/−180°, 30°–50°), as shown in Figs 3(c), (f), and (i), are formed by anti-apex meteoroids in high-inclined, prograde orbits, observed at around 6 PM. Those meteoroids travel at a higher speed than Earth, thus can be detected near dusk.

3.2 Dictionary

As discussed in the previous sections, simulation of each seasonal group contains between 100 and 500 million meteoroids. The whole simulation with three seasons comprises nearly 1 billion meteoroids. Even with a computer cluster, there are still constraints on the available memories of each computational node. The stochastic gradient descent process to be discussed in the next section requires information from all three seasons. Loading and accessing all 1 billion meteoroids at once are complex and slow. Searching operations within a vast data set is also inefficient. Alternatively, the I/O bottleneck, which leads to drastically worse performance, prevents us from dynamically loading those data on the fly. Our workaround is to create a dictionary, which in essence is a combination of a hash table and dynamic programming that allows quickly locating and retrieving all meteors from one batch. In this stage, meteoroids from each batch as described in the seeding process are pre-processed into a time-velocity (49 × 72) density histogram. Li & Zhou (2019) have discussed the configuration of the 2D histogram in greater detail. One 2D histogram, as shown in Fig. 4, contains meteoroids of one batch and is in the same configuration as the one shown in Fig. 2. The pre-processed data in the dictionary save many repetitive computations in subsequent steps and thus make the simulations computationally efficient. As discussed in the previous section, there are 263 536 pieces in the dictionary, each corresponding to a batch in the seeding process.

3.3 The solver

The solver's objective is to find the combination of the dictionary pieces that best match the observations. The solver uses stochastic gradient descent with selection and elimination to minimize the cost function. The cost function is defined as the relative density difference of the time-velocity density histogram between observation and the result constructed from simulation so that the number of selected dictionary pieces or meteoroids does not affect the cost function. The relative density is defined as the normalized 2D histogram shown in Fig. 2 and divided by its mean. It is inevitable to have multiple solutions due to a large number of degrees of freedom in the descending process. The solver reduces the degree of freedom by comparing the three seasonal groups simultaneously. In the solving process, the cost function must decrease or stay the same in all seasonal groups while adding or removing dictionary pieces. Hence, the solver can return consistent results in multiple independent runs. The final results, presented in Section 4, are the average of thousands of independent solutions. The solution process can be described as follows: In each step, the solver keeps selecting random pieces to

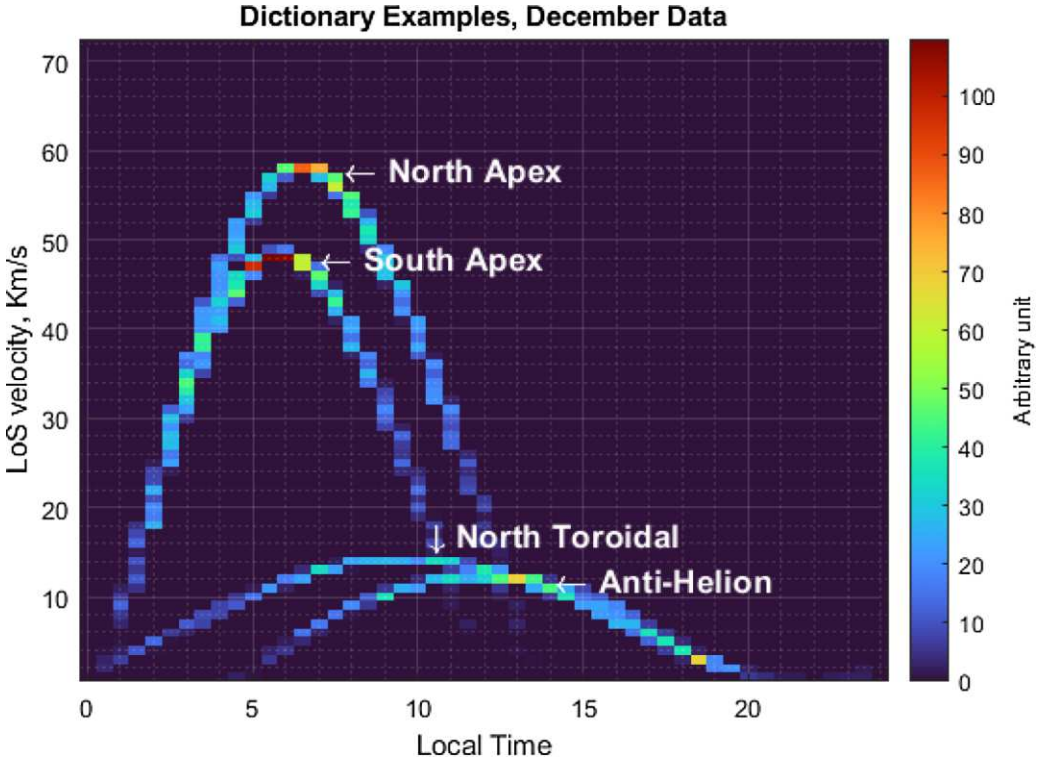

Figure 4. Examples of four different dictionary pieces. The time resolution is 30 min over 24 h, and velocity resolution is 1 km s^{-1} between 1 and 72 km s^{-1}. The sample is in arbitrary units. The example consists of meteoroids from North Apex (0° Lon. −30° Lat., 30 km s^{-1}, SRF; 0° Lon. −15° Lat., ERF), South Apex (0° Lon. 30° Lat., 30 km s^{-1}, SRF; 0° Lon. 15° Lat., ERF), North Toroidal (180° Lon. −30° Lat., 30 km s^{-1}, SRF; 0° Lon. −75° Lat., ERF), and Anti-Helion (160° Lon. 0° Lat., 30 km s^{-1}, SRF; 80° Lon. 0° Lat., ERF). The meteors in Fig. 4, especially those of Helion and Toroidal sources, only serve as examples of how a radiant source maps into the time-velocity diagram and do not represent the general meteor distribution of those sources. See detail in Section 3 and Fig. 9.

reduce the cost function. Until 500 pieces have been selected, the solver can either add one piece from the dictionary or remove one piece from chosen pieces if adding or removing the piece decreases the cost function. The solver keeps running until it cannot find a better solution after 5000 attempts. The cost function, on average, becomes less than 5 per cent of its initial state at the end of the solution process. Despite the chance of adding and removing being the same, the solution process is slightly in favour of adding more pieces. Thus, a typical final solution contains about 800 pieces, i.e. meteoroids from 800 directions, and speeds in a 2° spherical grid, from 10 to 40 km s^{-1} with 2 km s^{-1} incremental. It should be noted that the solving scheme is based upon the assumption that the overwhelming majority of the Arecibo meteors are detected in the main lobe or the inner sidelobes within a few degrees of the pointing direction. Although a recent study by Michell et al. (2019) indicates that roughly 25 per cent of the common meteors observed by radar and optical means are detected in the far sidelobes of a VHF radar, the much narrower mainlobe (1/6 deg) at Arecibo makes it very unlikely any appreciable amount of meteors are detected a few degrees off the beam centre. Additionally, the common meteors referred to in the study above are much larger meteors by at least several magnitudes and should be distinguished from the sporadic meteors in this work.

The most repetitive operation of the solver is matrix addition among a few hundred 49 × 72 matrices from the dictionary, which is computationally efficient. In other words, the solver can test millions of combinations within a short time. The gradient descent method could serve as an alternative to the stochastic selection/elimination process of the solver but with some disadvantages. The descending processes are often trapped in local minima with gradient descent, thus failing to converge. Also, calculating the gradient in the vector space with hundreds of thousands of dimensions can be time-consuming. Our numerical experiments found stepwise selection/elimination drastically outperforms gradient descent. The nature of a randomized and discrete stepwise method makes the solution process robust and less prone to local minima. Hundreds of consistent independent solutions from such a highly randomized process suggest the results are reliable.

3.4 Aspect sensitivity profile

Electromagnetic radiation from a highly irregular medium such as a meteor trail is highly anisotropic. It is reasonable to expect that radar observations of meteor head echoes are aspect sensitive. A decrease in meteor flux at near 6:00 AM Puerto Rico local time can be found on all three data sets. Referred to as the dip at 06:00 LT, this phenomenon was previously considered to be due to the Helion and anti-Helion sources (Janches et al. 2006; Fentzke & Janches 2008; Fentzke et al. 2009). One issue with these two sources is that they are low-speed meteors (see Fig. 9d non-inclined prograde meteors), whereas the missing flux is primarily due to the lack of high-speed meteors that must originate from the apex sources. One alternative explanation could be that the AO radar was not sensitive to down-the-beam meteors. To maintain the computational efficiency of the radiant direction solver, aspect sensitivity is incorporated into the dictionary by removing a portion of meteoroids according to their corresponding aspect angle. Each aspect sensitivity profile (ASP) is defined by three

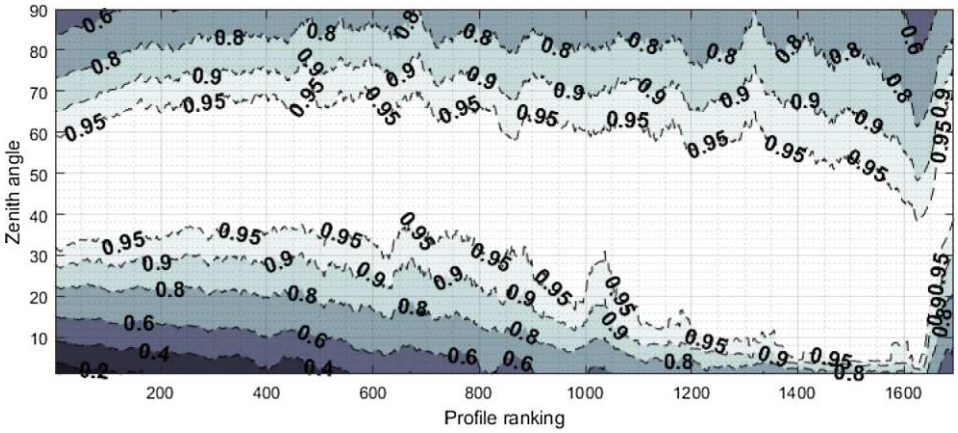

Figure 5. All ASPs in the best-to-worst order. The *x*-axis is the index of ASPs ranked from the best to the worst. The *y*-axis is the zenith angle, and the density/colour stands for sensitivity. Aspect sensitivity is calculated by considering the observations from all three seasonal groups.

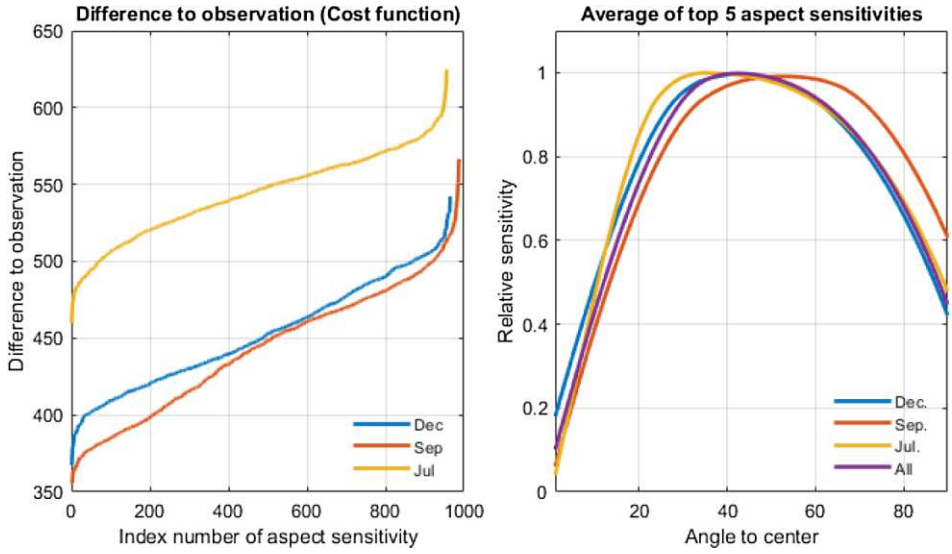

Figure 6. Fig. 6(a) (left) is the cost function by radiant direction solver from all 1694 ASPs, arranged from best to worst. *Y*-axis (cost function) is in arbitrary units. Fig. 6(b) (right) is the best aspect sensitivity of the three seasons that returns the lowest difference from the corresponding observation. Aspect sensitivity is solved independently. December and July data sets return identical best-fitting ASPs.

values: P0, P1, and P2. P0 and P2 are the values at 0° and 90° arrival angle and set between 0 and 1 with a step size of 0.1. P0 is the down-the-beam sensitivity, while P2 determines the sensitivity for the meteors perpendicular to the beam. P1 is the peak of the profile, which is always set to 1 with a to-be-determined angle between 5° and 70° with a step size of 5°. A shape-preserving piecewise cubic 1D interpolation then constructs the final ASP through those three points. We have built 1694 different ASP candidates that generally cover all possible ASPs with one peak. Then, the dictionaries constructed based on those ASPs are fed into the radiant distribution solver to find the one that returns the lowest cost function. The 1694 ASPs, arranged according to their performance, are shown in Fig. 5.

Our approach to find the best ASP is essentially an exhaustive search. The difference of the cost function associated with ASPs from the best to the worst is about 30 per cent, which is too shallow and almost certainly will trap the solver in local minima that is far from the optimal solution. On the other hand, the cost function associated with the radiant distribution can be reduced by about 95 per cent with stochastic selection/elimination. Our approach uses the solution of the radiant distribution as a vehicle to reveal the underlying effect of the ASPs. Additionally, the radiant distribution solver is written in dynamic programming that recursively uses the dictionary. Therefore, changing the ASP on the fly will drastically reduce computational efficiency.

The highly ranked ASPs from the three seasons and their trends show similar characteristics as depicted in Fig. 6(a), which shows the cost function for the best to the worst performing ASPs. The averages of the top five best ASPs are shown in Fig. 6(b). The best ASP indicates that the Arecibo radar is most sensitive to meteors with an arrival angle between 30° and 60°. The less sensitive range from zenith to about 30° could explain the meteor flux drop around dawn in the AO observations. The ASP differs from the meteor radar cross section derived from the Chemical Ablation Model (Janches et al. 2014), which indicates the detection probability of high-velocity meteors is close to one regardless the arrival angle. Nevertheless, we cannot find an alternative explanation other than aspect sensitivity that can account for the missing high-velocity meteors. The 'All' ASP shown in purple colour in Fig. 6(b) is used to solve the radiant

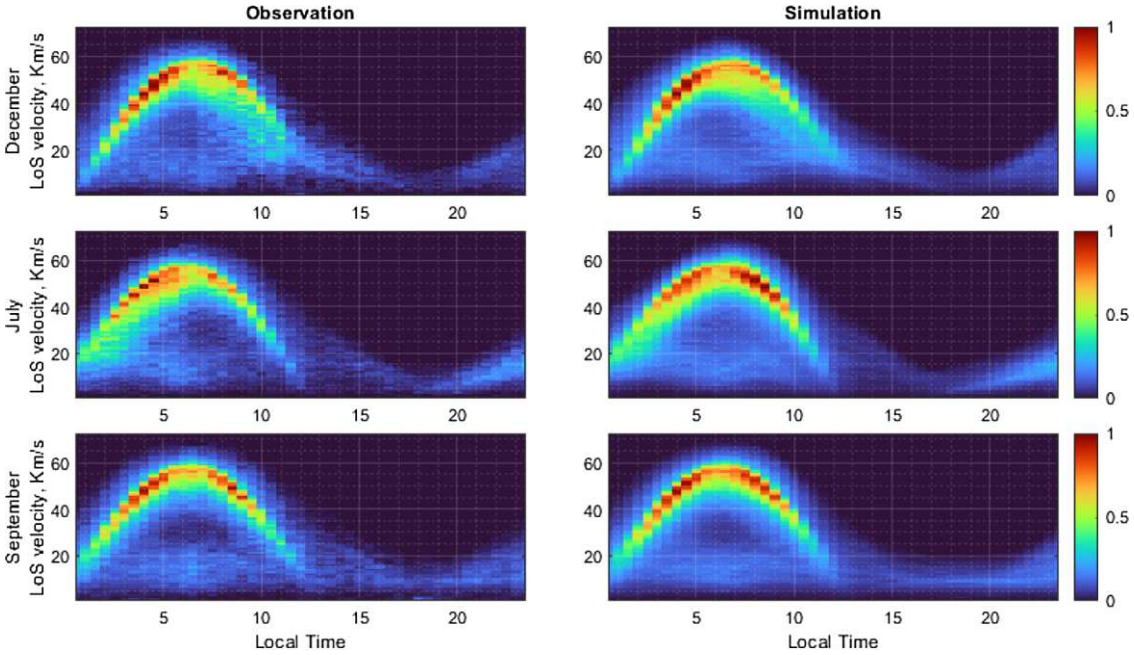

Figure 7. Comparison of observed and simulated time-velocity-density plots. The simulations are the average of ∼1000 independent solutions. The density of the figures is meteor flux in arbitrary unit/unit speed/unit time.

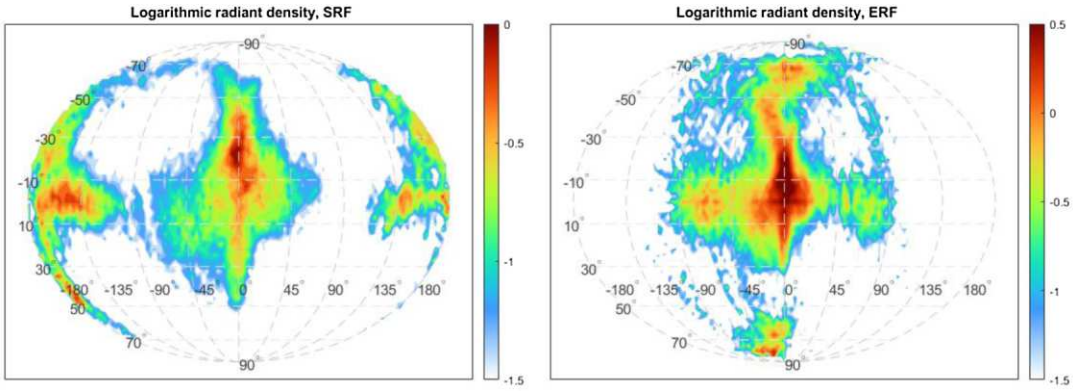

Figure 8. Logarithmic of the mean radiant density from ∼1000 independent solutions. Left-hand panel: distribution in the SRF; Right-hand panel: distribution seen in the ERF. The horizontal straight line that appears at the centre of the ERF figure is an artefact of the Mollweide projection.

distribution discussed in the following text. By considering AO's aspect sensitivity, the radiant density distribution obtained is likely a more accurate representation of the actual orbital distribution of meteoroids near Earth's orbit in the Solar system.

4 RESULTS

4.1 Raw radiant density distribution

Our goal for the algorithm is to determine the meteor radiant density distribution from the AO observations. The goal is achieved by comparing the observed and simulated time-velocity-density distributions. Fig. 7 compares the 2D time-velocity density histogram between simulation results generated from the radiant density and observations for the three seasonal groups. Among the several characteristics in Fig. 7, most notable is the main arc shape between mid-night and noon (hereafter referred to as the main arc). Another feature is the group of low-speed (∼10 km s^{-1}) meteors just below the main arc. The main arcs from the three seasons are in different shapes, as shown in Fig. 7. The July and December main arcs are asymmetric, with one 'leg' wider than the other. Also, the July and December results closely resemble each other if flipped along 6 AM. The shape of the arc is correlated to the radar pointing in the ecliptic latitude. The 'leg' is thinner or more concentrated when the radar is pointing to a lower ecliptic latitude and wider vice versa. The time variation of the radar pointing directions of September observations is symmetric with respect to 6 AM. The radar is pointed to a relatively low angle, 18° above the ecliptic at both mid-night and noon, so both legs of the main arc in September are relatively concentrated. The shape of the main arc is due to the basic trigonometric relationship between the radar pointing and meteors' incoming vector directions, as explained in Li & Zhou (2019). It is clear that the model captures the most prominent features in the observation.

Fig. 8 shows the logarithmic radiant density in the solar reference frame (SRF) on the left. The right-hand panel of Fig. 8 offers the same logarithmic radiant density but in the Earth reference frame

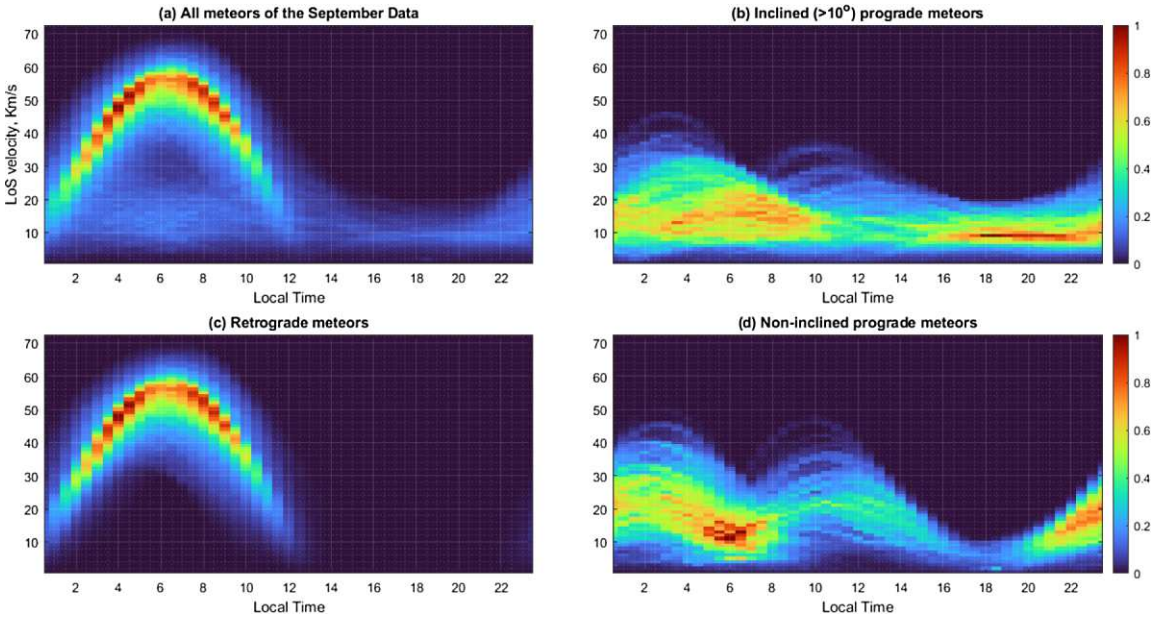

Figure 9. (a) 2D time-velocity density histogram of September observation. (b) Inclined (>10° ecliptic latitude) prograde meteors, which are those near the North and South Toroidal sources in ERF. (c) Retrograde meteors. (d) Non-inclined prograde meteors, which are commonly referred to as Helion and Anti-Helion meteors. All figures are normalized. The relative densities (colour scale) of inclined prograde meteors (b) and non-inclined prograde meteors (d) are about the same, with the latter being 103 per cent of the former.

(ERF), which takes Earth's orbital velocity into account. Meteors are seen to be pre-dominantly along 0° and 180° longitudes in SRF. Those meteors have their apogees and perigees near 1 au. In general, other radars have identified four source regions for meteors along 0° and 180° longitudes: North/South Apex at +/−15° latitude and North/South Toroidal at +/−50° latitude in the ERF. Although we see the North Apex source, the radiant density distribution at 0° longitude is more broadly distributed within +/−30° latitude in ERF. Due to the velocity transformation, the narrower spread within +/−30° latitude in ERF is stretched to about +/−60° in the SRF. Those meteoroids are on retrograde orbits and are responsible for the main arc in Fig. 7. They account for about 40 per cent of the total observed meteor flux. Unlike VHF radar observations (e.g. Kero et al. 2012), we cannot find a concentrated South Apex source as indicated in Fig. 8. If a concentrated South Apex source exists, it will be manifested as another arc slightly below the main arc in Fig. 7, as illustrated in Fig. 4. However, none of the observations show such a characteristic. As the South Apex source is as strong as the North Apex in other observations, a strong instrument selective effect likely exists at Arecibo.

We see two relatively concentrated sources centred at near 0° longitude and +/−65° latitude in ERF, which we will call high-latitude toroidal sources. Although they are easily visible in ERF, they are nowhere to be seen in SRF, as displayed in Fig. 8. According to our simulation, the high-latitude toroidal sources are merely an effect of coordinate transformation rather than actual sources. The high-latitude toroidal sources in ERF mainly consist of meteoroids in inclined prograde orbits caught by Earth. Meteoroids can be caught by Earth if their vector velocity component in the forward motion direction of Earth is slower than 30 km s^{-1}. For prograde meteoroids with a velocity around 30 km s^{-1}, Earth's orbital speed makes their observed velocity component in the ecliptic plane near zero, while the velocity component perpendicular to the ecliptic plan is unchanged from that in SRF. Those meteors are observed in either the high-latitude North or South Toroidal region, depending on their orbits in SRF. The meteors near the North or South Toroidal region but in the hemisphere of Anti-Apex consist of the meteoroids of the same radiant direction but travel faster than the Earth. Those are the low-speed meteors under the main arc in Fig. 7, also shown in the right-hand panel of Fig. 9.

Another group of meteoroids has their orbital plane close to the ecliptic. In ERF, those meteoroids are concentrated near +/−75° longitude, which is commonly referred to as Helion and Anti-Helion meteors. They are distributed beyond +/−130° ecliptic latitude in the SRF. The difference in longitude in ERF and SRF indicates that the Arecibo Helion and Anti-Helion meteoroids are primarily observed in prograde orbits.

Apart from the main arc of the apex meteors, two secondary arcs can be discerned in all plots in Fig. 7. The secondary arcs are more visible in the simulation results, which are shown in the right column of Fig. 7, as those results contain many more meteor events. The secondary arcs are roughly symmetric with respect to the apex direction, i.e. 6 AM, and intercept the main arc at 1 AM and 11 AM. Those interceptions are also approximately the peaks of the secondary arcs.

To better illustrate this point, we isolate the meteors of different radiant sources for September and plot them in Fig. 9 separately. It is evident from Fig. 9(d) that the non-inclined prograde meteors, which are those around the Helion and Anti-Helion sources in ERF, are the major constituents of the low-speed meteors in AO observations. Meteors that originated from the two secondary arcs overlap at 6 AM, accounting for the low-speed meteors found around 6 AM with a line-of-sight speed about 20 km s^{-1}. As shown in Fig. 9(b), the inclined prograde meteors also contribute to the AO low-speed meteors. They are also responsible for the meteors observed at dusk as there is a strong area between 4 PM and mid-night. In contrast to regions of high density, a triangular area with few meteors can be found between 4 AM and 9 AM, from 30 to 40 km s^{-1}, above the low-speed meteors and below the main arc in Fig. 9(a). This

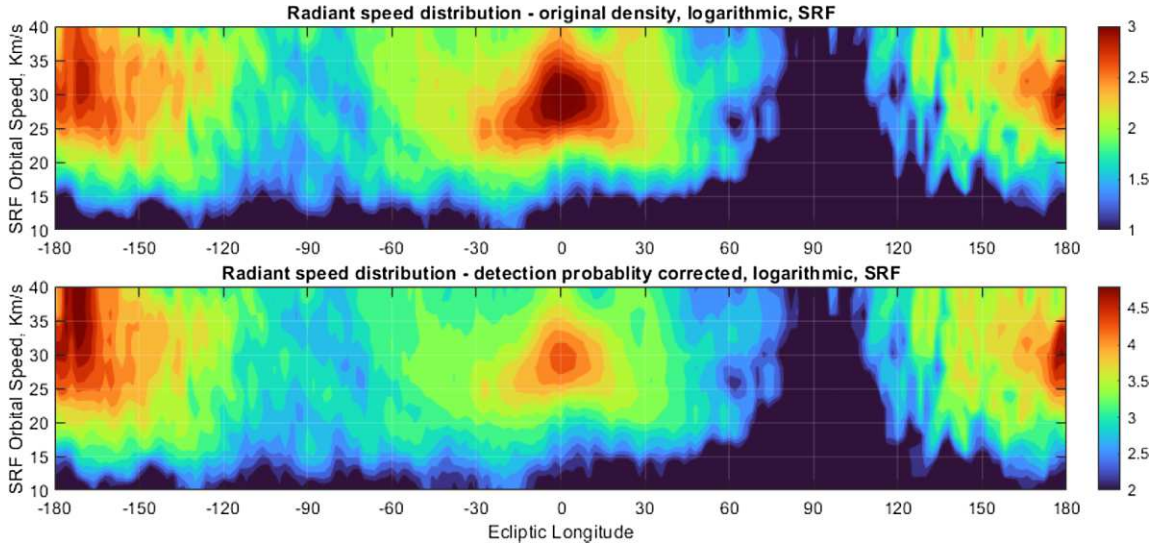

Figure 10. Radiant orbital speed distribution, original density (Fig. 10a, upper), and density with impact probability correction (Fig. 10b, lower). The impact probability correction is discussed in the second part of Section 4.

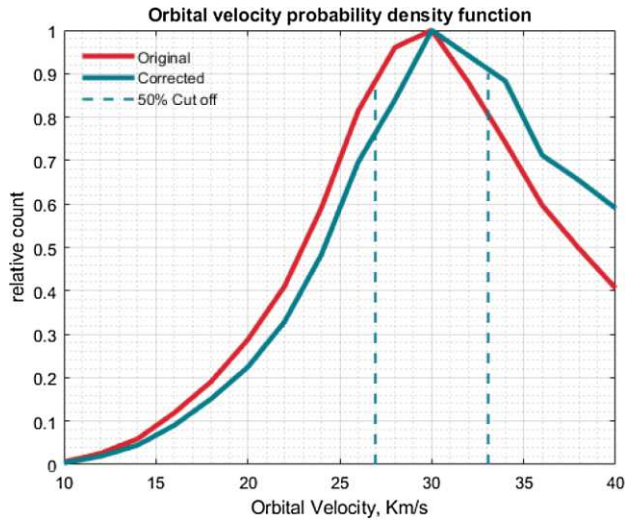

Figure 11. The relative orbital velocity density function of all meteors. The red curve is for meteors solved by the radiant distribution solver. The blue curve shows the density distribution with impact probability correction. The 50 per cent cut-offs of the two curves are nearly identical. The 50 per cent cut-off of both original and corrected PDF is marked by the two blue dashed vertical lines.

area corresponds to the void regions centred around along +/−90° longitude in the radiant distribution in the left-hand panel of Fig. 8.

Interception velocity at Earth's orbit is another essential aspect of the observed meteoroids. We plot the speed distribution by longitude in Fig. 10. A very strong peak can be found around 30 km s^{-1} at 0° longitude, i.e. in the Apex direction. Fig. 11 shows the speed distribution for all meteors observed. As seen from the figure, half of the meteors are within the speed range of about 30 +/− 3 km s^{-1}. When meteoroids have their apogee or perigee at the Earth's orbit, the orbital speeds between 27 and 33 km s^{-1} correspond to an eccentricity up to 0.22. The combined effect of Poynting–Robertson and the solar wind drags gradually reduces the eccentricity and the momentum of the interplanetary particles (Juhász 2013; Borin et al. 2017). Li & Zhou (2019) have preciously qualitatively concluded that the majority of the retrograde meteoroids are on quasi-circular orbits. The radiant distribution solver allows us to be more quantitative on the orbit characteristics of the meteoroids observed at Arecibo.

The mean orbital speed is the prime factor determining the Toroidal sources' actual location. For example, Kero et al. (2012) and Chau et al. (2007) report the Toroidal sources located near 55° ecliptic latitude using the MU and Jicamarca radars translate into a 25 km s^{-1} mean orbital speed. The orbital speed is derived using the transformation between ERF and SRF, and our simulation can also reproduce the same results. On the other hand, the radiant distribution based on AO observation suggests the Toroidal sources are near 70° ecliptic latitude. Our results indicate a 28 km s^{-1} mean orbital speed for the meteoroids responsible for the Toroidal sources. The model suggests that meteors detected at dusk in the AO campaign are travelling at a slightly faster orbital speed than those detected by MU and Jicamarca VHF radars.

4.2 Radiant density with impact probability correction

The radiant distribution shown in Fig. 8 is the observed result in the ERF with the instrument's aspect sensitivity taken into consideration. As shown in Fig. 3, the meteoroid radiant source distribution could be very biased as the impact probability varies by magnitudes among radiant sources. For example, meteoroids from the apex direction, i.e. 0° long. 0° lat., are several times more likely to hit the Earth than those coming from the opposite direction. Therefore, observing more meteors from a certain radiant source does not necessarily imply the corresponding radiant source is more abundant when viewed in the SRF. The orbital speed of Earth is the leading cause of the observation bias. Retrograde meteors when combined with Earth's vector speed makes the Earth visible to a more extensive range of orbital parameters. For meteors in prograde orbits, the effect is the opposite. The impact probabilities of the three seasons have been discussed in the seeding section and are shown in Fig. 3.

The observation bias can be reduced by dividing the radiant density distribution by the impact probability. The radiant source distribution with the impact probability corrected is shown in Fig. 12. The radiant orbital speed distribution with the observation bias correction is shown in Fig. 10(b). With impact probability correction, the result

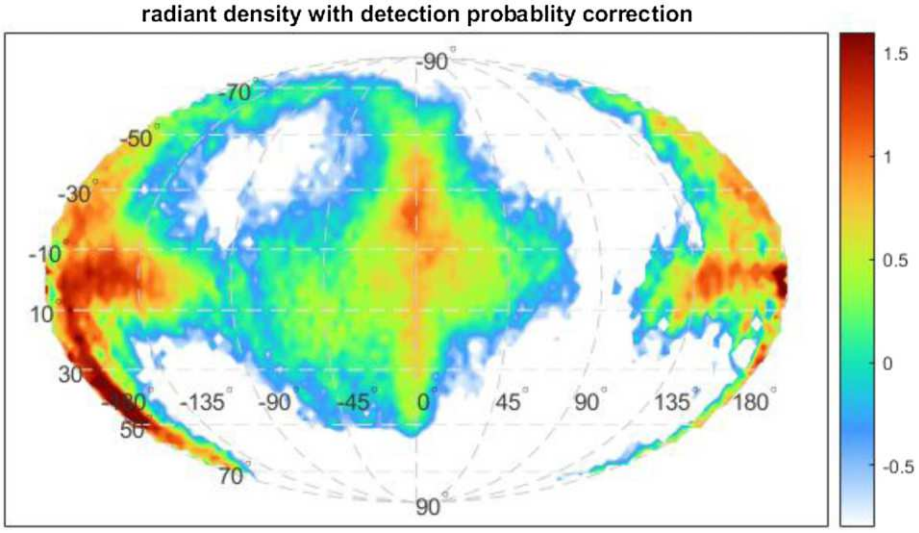

Figure 12. Radiant density with impact probability correction. Impact probability correction reduces observation bias and results in a more accurate representation of the orbital distribution of the interplanetary particles.

indicates about 75 per cent of the total meteoroid population are travelling on prograde orbits. The corrected radiant distribution shows that there are more prograde meteors than retrograde meteors, which is contrary to the apparent rate of the observations. The impact probability corrected radiant density distribution is more compatible with the nebular hypothesis that describes the Solar system's formation. The nebular hypothesis suggests most particles and all the planets in the Solar system are travelling in the same direction.

5 CONCLUSION

In this work, we have developed a special stochastic stepwise descend procedure that solves the radiant distribution of AO meteors. The algorithm solves the AO radiant source distribution based on observations from three seasons with over 250 000 meteor echoes. Five out of six primary meteor sources can be identified in the radiant distribution. We do not find a concentrated source in the South Apex region. Instead, the result shows a spread Apex source broadly distributed between $+/-50^\circ$ ecliptic latitudes with the maximum density near 25°N.

We have compared the radiant source distribution between ERF and SRF and discussed the orbital characteristics of each of the six sources. To summarize, the Apex sources almost only consist of retrograde meteors; Helion and Anti-Helion sources consist of prograde meteoroids travelling near the ecliptic plane; North and South Toroidal sources are primarily formed by prograde Anti-Apex meteoroids with inclined orbits. Further, retrograde meteors observed at AO are dominated by meteors in circular inclined orbits.

We discuss how the observed time-velocity-density characteristics are related to the meteoroid orbital parameters. The low-speed meteors detected around 6 AM in AO are meteoroids in prograde non-inclined orbit, and the main arc is almost purely constituted by retrograde meteoroids around the North Apex region. Our algorithm finds the Arecibo radar is most sensitive to meteors arriving between 30° and 60° to the beam pointing direction and not sensitive to down-the-beam meteors and meteors arriving perpendicular to the beam. This characteristic explains the depression of high-speed meteor flux around 6 AM.

We also report the impact probability in all directions and the radiant source distribution corrected for the impact probability. The corrected radiant source distribution suggests that about 75 per cent of meteoroids travel in the same direction as Earth. There are almost twice as many particles in Anti-Apex direction as in Apex direction. This conclusion is more compatible with the established theory of the formation of the Solar system (Hyashi et al. 1985) and provides new insight into meteoroid orbital study. The AO meteor radiant source distribution derived by our algorithm appears to be self-consistent and can explain many key features in the observed time-velocity-intensity distribution.

ACKNOWLEDGEMENTS

The Arecibo Observatory is a facility of the National Science Foundation operated under cooperative agreement with the University of Central Florida. The study is partially supported by NSF grants AGS-1744033, AGS-2152109, and AGS-1903346. The raw data used for the analysis can be obtained from the Arecibo Observatory. T-YH acknowledges that her work is supported by (while serving at) the National Science Foundation. Any opinion, findings, and conclusions or recommendations expressed in this material are those of the authors and do not necessarily reflect the views of the National Science Foundation.

DATA AVAILABILITY

The raw data used for this study can be obtained from the Arecibo Observatory data archive.

REFERENCE

Babadzhanov P., Obrubov Y. V., 1992, Dynamics and Evolution of Minor Bodies with Galactic and Geological Implications. Springer, Berlin, New York, p. 111
Borin P., Cremonese G., Marzari F., Lucchetti A., 2017, A&A, 605, A94
Campbell-Brown M., Jones J., 2006, MNRAS, 367, 709
Chau J. L., Woodman R. F., Galindo F., 2007, Icarus, 188, 162
Chivers I., Sleightholme J., 2015, Introduction to programming with Fortran. Springer, Berlin, New York, p. 359

Close S., Oppenheim M., Hunt S., Dyrud L., 2002, J. Geophys. Res., 107, SIA 9–1
Fentzke J. T., Janches D., 2008, J. Geophys. Res., 113, A03304
Fentzke J., Janches D., Sparks J., 2009, J. Atmos. Sol. Terr. Phys., 71, 653
Hairer E., Lubich C., Wanner G., 2003, Acta Numer., 12, 399
Halliday I., Blackwell A. T., Griffin A. A., 1990, Meteoritics, 25, 93
Hayashi C., Nakazawa K., Nakagawa Y., 1985, Protostars and Planets II. University of Arizona Press, Tucson, AZ, p. 1100
Janches D., Nolan M. C., Meisel D. D., Mathews J. D., Zhou Q. H., Moser D. E., 2003, J. Geophys. Res., 108, 1222
Janches D., Heinselman C. J., Chau J. L., Chandran A., Woodman R., 2006, J. Geophys. Res., 111, A07317
Janches D., Plane J., Nesvorn`y D., Feng W., Vokrouhlick`y D., Nicolls M., 2014, ApJ, 796, 41
Juhász A., Horányi M., 2013, Geophys. Res. Lett., 40, 2500
Kero J. et al., 2012, MNRAS, 425, 135
LeCun Y. A., Bottou L., Orr G. B., Müller K.-R., 2012, Neural networks: Tricks of the trade. Springer, Berlin, New York, p. 9
Li Y., Zhou Q., 2019, MNRAS, 486, 3517
Li Y., Zhou Q., Scott M., Milla M., 2020, J. Geophys. Res., 125, e2019JA027459
Mathews J. D., Janches D., Meisel D. D., Zhou Q. H., 2001, Geophys. Res. Lett., 28, 1929
Mathias D. L., Wheeler L. F., Dotson J. L., 2017, Icarus, 289, 106
Michell R., DeLuca M., Janches D., Chen R., Samara M., 2019, Planet. Space Sci., 166, 1
Nesvorný D., Vokrouhlický D., Pokorný P., Janches D., 2011, ApJ, 743, 37
Pellinen-Wannberg A., Westman A., Wannberg G., Kaila K., 1998, Ann. Geophys., 16, 1475
Pokorný P., Vokrouhlický D., Nesvorný D., Campbell-Brown M., Brown P., 2014, ApJ, 789, 25
Plane J., 2004, Atmos. Chem. Phys., 4, 627
Schult C., Kero J., Stober G., Brown P., 2021, Icarus, 355, 114137
Seal R., Urbina J., 2020, IEEE Aerosp. Electron. Syst. Mag., 35, 30
Sulzer M., 2004, Atmos. Chem. Phys., 4, 947
Szasz C., Kero J., Meisel D. D., Pellinen-Wannberg A., Wannberg G., Westman A., 2008, MNRAS, 388, 15
Wheeler L. F., Mathias D. L., Stokan E., Brown P. G., 2018, Icarus, 315, 79
Witze A., 2020, Nature, 587, 529
Yue X. et al., 2020, Earth Planet. Phys., 4, 579
Zhou Q. H., 2000, Geophys. Res. Lett., 27, 1803
Zhou Q., Tepley C. A., Sulzer M. P., 1995, J. Atmos. Terr. Phys., 57, 421
Zhou Q. H., Mathews J. D., Nakamura T., 2001, Geophys. Res. Lett., 28, 1399

This paper has been typeset from a Microsoft Word file prepared by the author.